Journal of the Geological Survey of Brazil

Fluid inclusion and isotope (O, H, C, Sr) constraints on the orogenic gold mineralization at the Enche Concha and Tunel prospects, Gurupi Belt, Brazil

Reinaldo Fontoura de Melo Junior[1,2*], Evandro L. Klein1[2,3], Jean Michel Lafon[1], Chris Harris [1,2]

[1] Programa de Pós-Graduação em Geologia e Geoquímica, Universidade Federal do Pará, Cidade Universitária José da Silveira Netto - Campus Básico, Avenida Augusto Corrêa 01, Belém-PA, Brazil, CEP: 66075-110
[2] GPGE – Grupo de Pesquisa em Geologia Econômica, Programa de Pós-Graduação em Geologia e Geoquímica, Universidade Federal do Pará, Belém, Brazil
[3] Geological Survey of Brazil/ CPRM. SBN quadra 2, bloco H Ed. Central Brasília. Asa Norte, Brasília-DF, CEP: 70.040-904. Brazil
[4] - Department of Geological Sciences, University of Cape Town, Rondebosch, South Africa

Abstract

The gold mineralization at the Enche Concha and Tunel prospects, northwestern portion of the Gurupi Belt, is hosted in dacites and phyllites that belong to the ca. 2160 Ma-old metavolcano-sedimentary Chega Tudo Formation. These host rocks are variably deformed, from a spaced cleavage to schistose and mylonitic varieties. The hosting structures have previously been defined as produced in the Paleoproterozoic. The hydrothermal alteration processes include carbonatization, sericitization, sulfidation, and quartz veining. These processes are both pervasive and fissure-filling in style. Pyrite is largely predominant over chalcopyrite and sphalerite and gold occurs as a refractory phase in pyrite. Fluid inclusion, stable (O, H, C) and Sr isotopes studies indicate that the hydrothermal alteration and gold mineralization occurred between 260 and 370°C (mostly ~328°C), and 0.85 to 2.8 kbar, from a low-salinity (~5% NaCl), aqueous-carbonic (XCO_2 = 0.03-0.13), relatively reduced (log fO_2 = -32.1), and near neutral (pH = 5.0-6.2) metamorphic fluid ($\delta^{18}O$ = +9.4 to +11.3‰, δD = -25 to -28‰). Contributions from deep-seated (lower crust and mantle) sources are suggested by a $\delta^{13}CCO_2$ value of -7.6‰, and $^{87}Sr/^{86}Sr$ ratios between 0.702699 and 0.705141, which are lower than those found in the country rocks. Gold was transported by the $Au(HS)_2$- complex and precipitation occurred in response to phase separation, identified by fluid inclusions, and fluid-rock interactions, given by the lowering of the $\delta^{13}CCO_2$ values. The geological and genetic characteristics are equivalent to those of the orogenic gold system previously defined for the Gurupi Belt.

Article Information

Publication type: Research paper
Received 16 October 2019
Accepted 9 July 2020
Online pub. 27 July 2020
Editor(s): Vladimir Medeiros

Keywords:
Orogenic gold,
Sr isotopes,
stable isotopes,
metallogenesis,
hydrothermal alteration,
Paleoproterozoic

*Corresponding author
Reinaldo Fontoura de Melo Junior
E-mail address: reinaldofmjr@hotmail.com

1. Introduction

The Gurupi Belt, in northern Brazil, contains shear zone-hosted gold deposits that totalize over 158 t of gold (~5 Moz). These deposits, including Cachoeira, Chega Tudo, and Cipoeiro, have been defined as belonging to an orogenic gold system (Klein 2014), and formed at the late stages of an accretionary-collisional Rhyacian orogeny (Klein et al. 2020; Tavares et al. 2017). Enche Concha and Tunel are exploration targets (prospects, separated by ca. 2.4 km) located in the central portion of the Gurupi Belt (Fig. 1) and they have received intermittent exploration work. Unpublished company reports inform the presence of several mineralized intersections, most notably 3.5 m @ 0.82 g/t at Enche Concha, and 7.39 m @ 0.83 g/t (including 1 m @ 2.50 g/t) in the Tunel prospect.

Although the orogenic model is well-defined for the Gurupi Belt, no information on host rocks, hydrothermal alteration, and genetic aspects for several prospects, including Enche Concha and Tunel, is available. In this work, we discuss these aspects for both prospects, supported by fluid inclusions, stable isotopes (C, O, H), and provide the first Sr isotope compositions of hydrothermal calcite associated with gold mineralization in the Gurupi Belt. The results allow us to discuss the physico-chemical characteristics and sources of the mineralizing fluid, and make comparisons with known deposits in the Gurupi Belt and elsewhere.

2. Geological setting and gold metallogeny

2.1. Regional geology

The Gurupi Belt is composed of magmatic, sedimentary and metamorphic rocks that range in age from 2695 Ma to 549 Ma (Fig. 1, Klein et al. 2020, and references therein). The oldest rock is the Archean Igarapé Grande metatonalite (2695 ± 4 Ma), which forms part of the basement of the belt. Most of the rock units were formed during the Rhyacian period and include arc-related sequences, such as the orthogneisses of the Itapeva Complex (2167-2148 Ma), voluminous juvenile calc-alkaline granitoids of the Tromaí Intrusive Suite (2174-2148 Ma) and Canoa quartz diorite (2162 ± 11 Ma), amphibolites (2166-2136 Ma), the juvenile metavolcano-

ISSN: 2595-1939
https://doi.org/10.29396/jgsb.2020.v3.n2.2
Open access at jgsb.cprm.gov.br

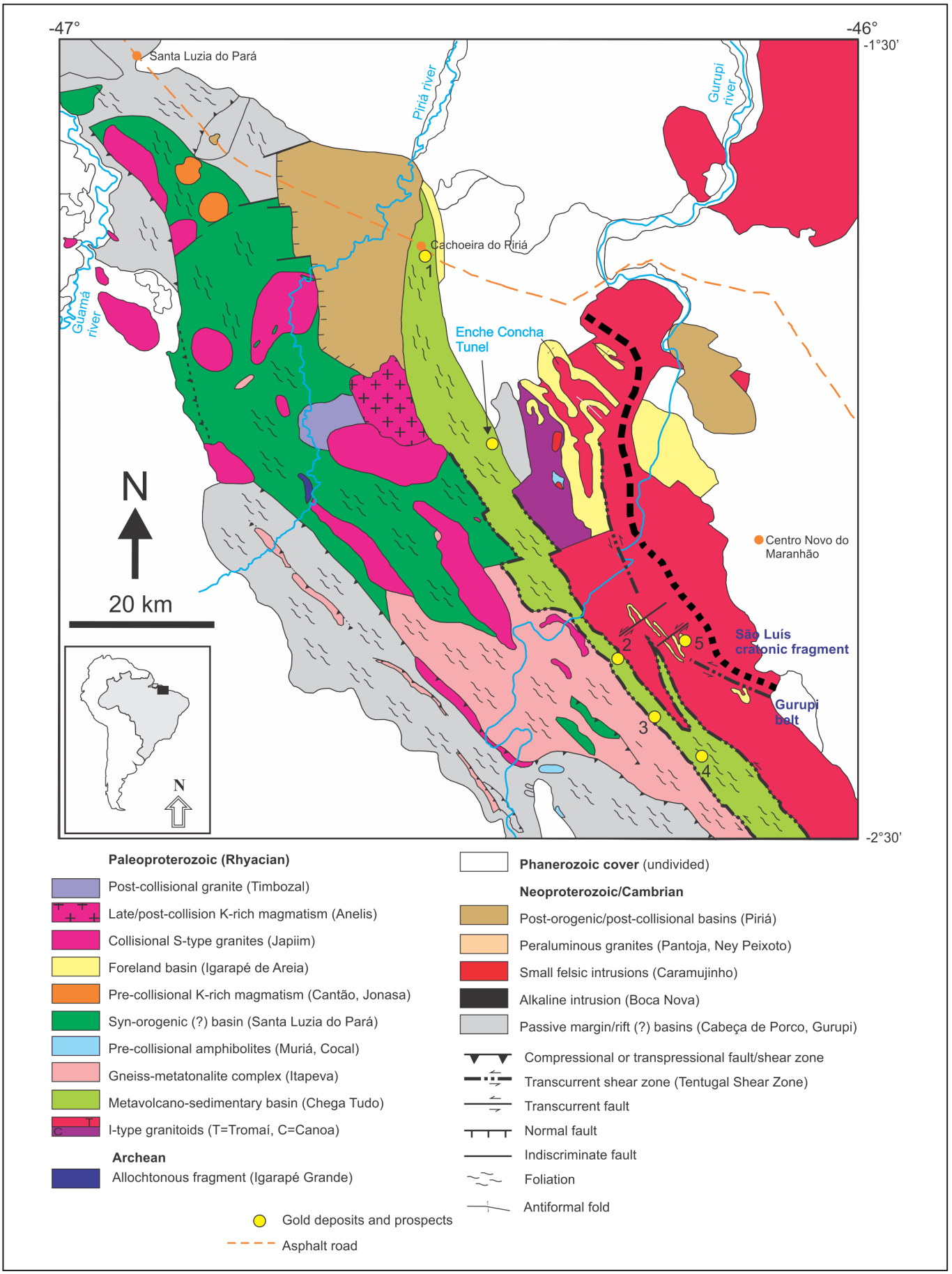

FIGURE 1. Location map (inset) and simplified geological map of the Gurupi Belt (modified from Klein et al. 2020), with location of the Enche Concha and Tunel prospects and main gold deposits: 1 – Cachoeira, 2 – Chega Tudo, 3 – Serrinha, 4 – Montes Áureos, 5 – Cipoeiro.

sedimentary Chega Tudo Formation (2160 ± 3 to 2146 ± 1 Ma), and the potassic and weakly peraluminous granitoids of 2163 ± 4 Ma (Cantão), 2142 ± 9 Ma (Jonasa), which show crustal signature. Variably deformed peraluminous, muscovite- and biotite-bearing granites and leucogranites with ages between 2116 Ma and 2072 Ma and with crustal signature (Japiim Intrusive Suite) are related to the collisional phase of the Rhyacian orogeny; whereas highly evolved to shoshonitic granite and quartz-syenite of 2100 ± 21 Ma (Anelis Suite), and potassic granite of 2084 ± 5 Ma (Timbozal Granite) are post-collisional units (Klein et al. 2020). Siliciclastic sequences are included in orogenic sedimentary basins, such as the Santa Luzia do Pará Formation (younger than 2140 Ma) and the Igarapé de Areia Formation (younger than 2078 Ma) (Klein et al. 2020). All these Rhyacian units are part of an accretionary to collisional orogen, which continues to the north in the São Luís cratonic fragment (Klein et al. 2020, and references therein).

Neoproterozoic units comprise siliciclastic metasedimentary rocks younger than 1140 Ma (Gurupi Group) and 630 Ma (Piriá Formation), an anorogenic intrusion of nepheline-syenite (732 ± 7 Ma), a calc-alkaline metatonalite (624 ± 16 Ma), and peraluminous, two-mica granites (Ney Peixoto and Pantoja granites) of 549 ± 4 Ma (Klein et al. 2020, and references therein).

In terms of structural evolution, Tavares et al. (2017) defined three phases for the Gurupi Belt. (1) D_1 is ductile, oriented predominantly to N40°-50°W, progressively folded by D1b, and coeval to the peraluminous granites of ca. 2100-2070 Ma. The development of the Tentugal shear zone is associated with this phase. (2) D_2 is also ductile, affecting only Paleoproterozoic rocks, and strikes WNW-ESE to E-W. (3) D_3 affects both Paleoproterozoic and Neoproterozoic rocks, with direction averaging N-S. The Tentugal shear zone was reactivated in this phase.

2.2. Summary of gold metallogeny

According to Klein (2014), the orogenic gold deposits of the Gurupi Belt are hosted in Paleoproterozoic (2160-2147 Ma) metavolcano-sedimentary and calc-alkaline granitic rocks formed in magmatic arc and/or back-arc settings during a Rhyacian orogeny (2240-2080 Ma) (Fig. 1). The distribution of the gold deposits is controlled by the Tentugal shear zone and its subsidiary structures, which were developed during the D1 deformation phase (Tavares et al. 2017) and broadly coeval to the intrusion of collision-type peraluminous granites at ca. 2100-2070 Ma. The hydrothermal alteration comprises varied amounts of sericite, chlorite, carbonate minerals and sulfides. Gold occurs in quartz and quartz-carbonate veins (with or without sulfides) and in association with disseminated sulfides in strongly altered and variably deformed host rocks. Gold precipitation occurred mostly between 300 and 370°C and up to 3 kbars in response to fluid immiscibility and fluid-rock reactions and minor fluid mixing and oxidation. Geological characteristics, petrographic, fluid inclusion, and isotopic evidence indicate near-neutral, reduced aqueous-carbonic metamorphic fluids, with local contributions from host rocks at the deposit site (Klein 2014, and references therein).

3. Analytical procedures

All studies were performed in samples obtained from three drill cores. The fluid inclusion studies were carried out in the Laboratório de Microtermometria of the Federal University of Pará (UFPA), in Belém, Brazil, using a Linkam MDSG600 heating-freezing stage with a temperature range of −196° to 600°C. The calibration was done with synthetic fluid inclusions containing pure CO_2 (melting at -56.6 ºC) and H_2O (melting at 0.0 ºC). The precision was estimated at ± 0.5º C and ± 5ºC for temperatures lower and higher than 50ºC, respectively. The analytical procedures followed criteria from Roedder (1984), Shepherd et al. (1985), and Goldstein and Reynolds (1994). Physical and chemical properties were estimated with the software FLINCOR (Brown 1989), following the equations of Brown and Lamb (1986) for pure H_2O and CO_2 system, and Bowers and Helgeson (1983) for the H_2O-CO_2-salt system.

Regarding the stable isotopes, the carbon and oxygen isotope compositions of calcite were carried out in the Laboratório de Isótopos Estáveis of the University of Brasília, Brazil, using the continuous flow approach. After cleaning of the samples in a He flux at about 72°C, the CO_2 was obtained in a vacuum line by reaction with H_3PO_4 at 25°C, and subsequently purified cryogenically. The isotope compositions were measured with triple collectors of a SIRA II mass spectrometer. Oxygen isotopes in quartz and hydrogen isotopes in fluid inclusions were analyzed in the Stable Isotope Laboratory of the Department of Geological Sciences, University of Cape Town, South Africa. The isotope ratios were measured off-line using a Finnigan Delta XP mass spectrometer in dual inlet mode. Oxygen was analyzed by the laser fluorination method described by Harris and Vogeli (2010). Oxygen from quartz was liberated after reaction with BrF5 and conversion to CO_2 by reaction with graphite at 750°C. An internal standard (Monastery garnet – MONGT, $\delta^{18}O$= +5.55‰) was analyzed to calibrate the data to the V-SMOW (Vienna Standard Mean Ocean Water) scale. Hydrogen isotopes were also measured on fluid inclusion water extracted from quartz vein samples by thermal decrepitation of the fluids inclusions. The quartz vein fragments were degassed under vacuum at 200°C using a hot air gun to eliminate any moisture before heating it to about 800 °C. The obtained water was trapped cryogenically and transferred to pyrex tubes containing Zn. The hydrogen isotope composition of the H_2O was determined using the closed tube Zn reduction method of Vennemann and O'Neil (1993), and the internal water standard CTMP2010 and RMW were used to calibrate the data to the V-SMOW scale. The stable isotope results are reported in ‰ in the delta notation ($\delta^{18}O$, δD, $\delta^{13}C$) relative to the V-SMOW (oxygen, hydrogen), and V-PDB (Vienna Pee Dee Belemnite, carbon) scales.

Strontium isotopic analyses were carried out at the Laboratório de Geologia Isotópica (Pará-Iso) of the UFPA. About 500 mg of powdered sample was first washed with ultrapure water and dissolved with 150 µl of HCl 2N distilled twice, until reaction was over. Extraction and purification of Sr were carried out by ion-exchange chromatography using a Eichrom® Sr 50–100 µm resin, conditioned in HNO_3 medium followed by ultrapure water as eluant. The Sr concentrates were loaded on degassed tungsten single filament. The Sr isotopic ratios were measured on a Finnigan MAT 262 thermal ionization multi-collector mass spectrometer (TIMS) and they were corrected from mass discrimination using $^{84}Sr/^{88}Sr$ = 0.1194. During the period of Sr isotopic determinations, the accuracy, precision, and reproducibility of the analyses were monitored by repeated measurements of the NBS987 reference material.

4. The Enche Concha and Tunel prospects

4.1. Host rocks

Petrographic investigation of drill cores down to 265 m in depth allowed the recognition of different rock types hosting hydrothermal alteration and gold mineralization. The rocks comprise an intercalation of dacite and phyllite, along with brecciated zones (Fig. 2).

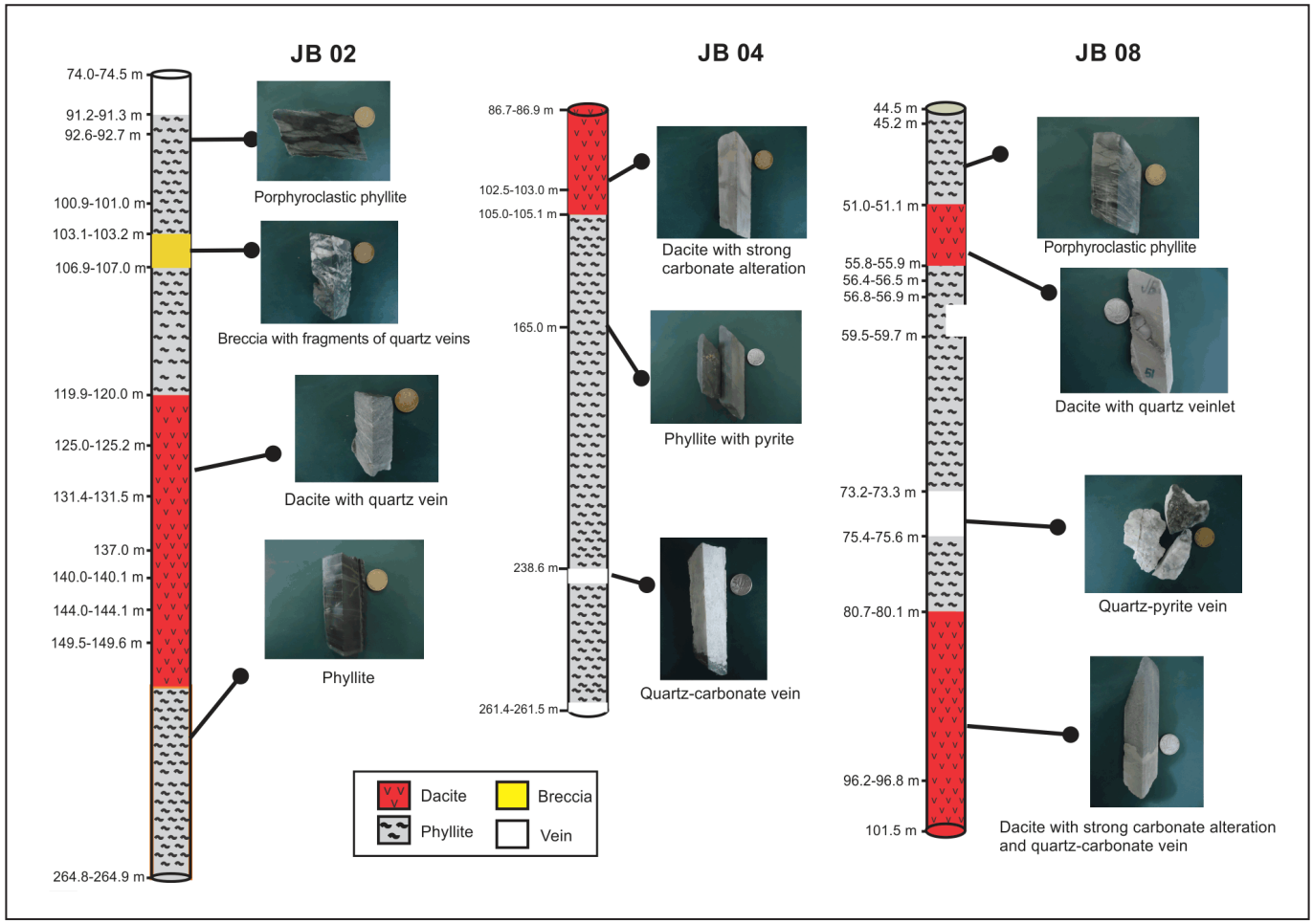

FIGURE 2. Schematic sections based on drill cores for the Enche Concha (JB02, JB04) and Tunel (JB08) prospects, with photographs of representative rock types.

The phyllite is a dark grey to greenish rock (Figs. 2 and 3A) composed of quartz, white mica, chlorite, and carbonate. This rock shows a penetrative and continuous cleavage, which gradually pass to a spaced foliation defined by the alternation of thin layers of mica and quartz. Locally, the rocks resemble schists, where the minerals are recrystallized and coarser-grained (Fig. 4). Porphyroclastic texture is also observed, with ovoid fragments of carbonate that are contoured by fine-grained micas and quartz (Fig. 4C). The variation in the planar structures may indicate progressive deformation (S1 followed by $S1_b$, according to Tavares et al. 2017).

The dacites are light grey rocks with variable grain size, from aphanitic, to fine-grained and locally porphyritic (Figs. 2 and 3B). The granular varieties are composed of plagioclase (75%) and quartz (25%). The plagioclase is tabular and euhedral to subhedral (Figs. 3B and 4H), and partially replaced by carbonate (Fig. 4J). The quartz grains are anhedral and show subgrains. In the porphyritic varieties, which are also porphyroclastic due to deformation, the phenocrysts/porphyroclasts made up 25% of the rocks, and comprise plagioclase (20%) and quartz (5%) set in a quartzo-feldspathic matrix (Figs. 4K, 4L). The plagioclase is anhedral to subhedral, rather ovoid, and strongly replaced by sericite and carbonate (Fig. 4), whereas quartz is anhedral and rounded.

The fault breccia forms centimeter-thick layers that cut across the phyllite and dacite layers. The rocks are fragmentary, non-cohesive, and without evident planar tectonic fabric (Fig. 3C). The fragments consist of vein quartz, vein carbonate and phyllite (Figs. 4M, 4N), which range in shape from angular to rounded, immersed in a quartzo-feldspathic matrix (20% of the breccia volume), which locally contains carbonate cement.

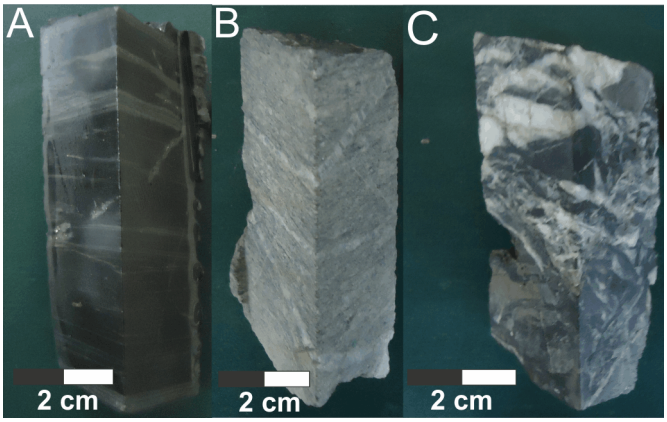

FIGURE 3. Drill core images of host rocks from the Enche Concha and Tunel prospects. (A) Phyllite showing alternating dark (chlorite) and whitish (quartz, mica, carbonate) laminae, crosscut by thin veinlets of carbonate. (B) Dacite with porphyroclastic texture exhibiting quartz and plagioclase porphyroclasts. (C) Breccia with quartz cementing angular fragments of dark phyllite.

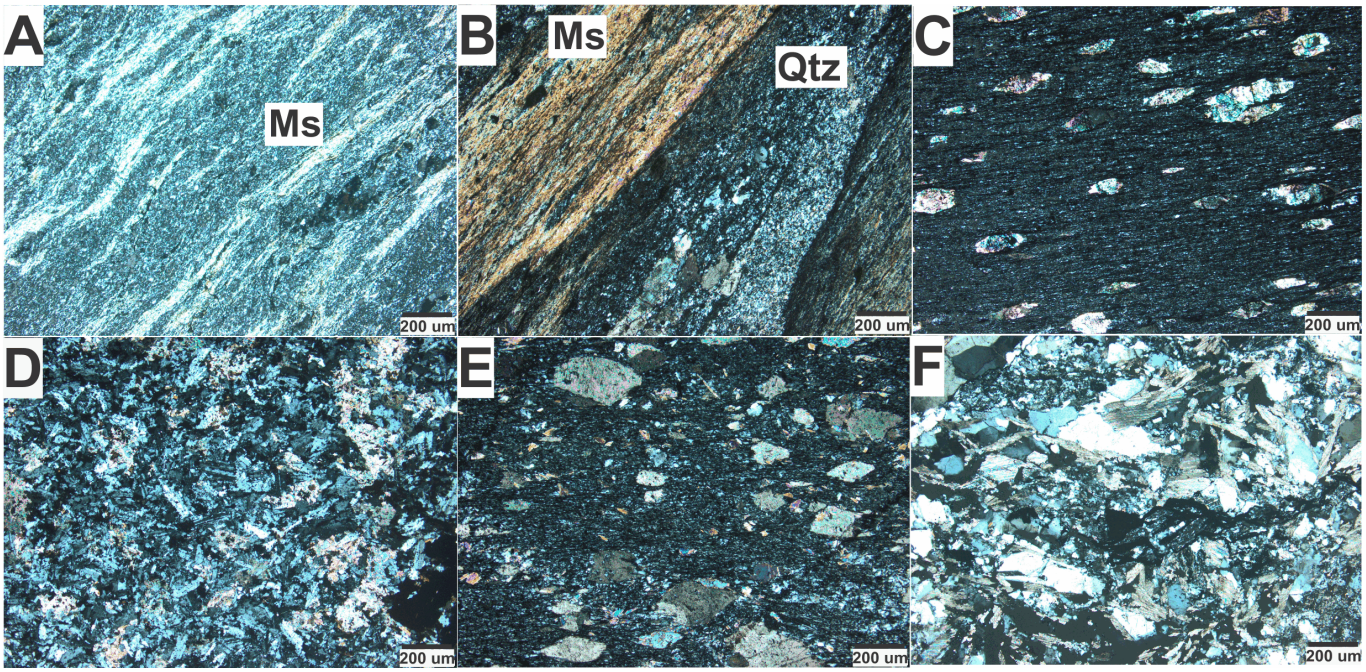

FIGURE 4. Photomicrographs of host rocks of the Enche Concha and Tunel prospects taken with crossed nicols. (A) Phyllite with continuous cleavage grading to foliation marked by muscovite crystals. (B) Foliated/laminated phyllite with muscovite- and quartz-rich laminae. (C) Deformed (porphyroclastic) phyllite with ovoid porphyroclasts of plagioclase partially replaced by carbonate. (D) Dacite with subhedral granular texture showing twinned plagioclase crystals. (E) Dacite porphyry, with deformed phenocrysts of plagioclase partially replaced by carbonate. (F) Breccia with fragments of quartz and carbonate without apparent ductile fabric. Mineral abbreviations: Ms – muscovite, Qtz – quartz.

4.2. Hydrothermal alteration and gold mineralization

The hydrothermal alteration comprises four processes: carbonatization, sericitization, sulfidation, and quartz veining. These processes are both pervasive and fissure-filling, are distributed in all host rocks and have slightly different timing regarding deformation (Fig. 5).

Carbonatization is the main and more widespread alteration process observed in all lithotypes and along the entire investigated depths. The carbonate alteration comprises the formation of anhedral calcite, with grain-size ranging from 0.5 to 1.0 mm, and two types/stages are observed: (1) disseminated, by replacement of the magmatic plagioclase (Figs. 6A, 6B), and (2) crystallization in mm-thick veinlets (Fig. 6C). The veining is more intensive in the more deformed portions of the host rocks.

The sericitic alteration occurs predominantly in the dacites and is present in different forms. The alteration is mainly placed along the foliation planes (Fig. 6D), being syn-tectonic to S1 or S1b. Sericite in pressure shadows of pyrite (Fig. 6E) indicates crystallization during the late stages (S1b?) of foliation development (Witt 1993). Locally, the sericite flakes cut across plagioclase crystals, which are partially or completely replaced by carbonate (Fig. 6F). Disseminated patches and replacement of plagioclase are also common (Fig. 6G).

The sulfide alteration affects all host rocks, but is more abundant in the phyllites and quartz veins, being probably associated with the late stages of the ductile deformation. Pyrite is largely the predominant sulfide phase, with subordinate amounts of sphalerite and chalcopyrite occurring in spatial association with pyrite (Fig. 6H). Thin layers of pyrite are placed along the foliation planes or cut across this foliation (Figs. 6I, 6J), and isolated euhedral crystals associated or not with carbonate are also common (Figs. 6K, 6L).

Veins and veinlets of quartz and quartz-carbonate, with or without sulfides (Figs. 6I, 6K, 6L), crosscut all lithotypes.

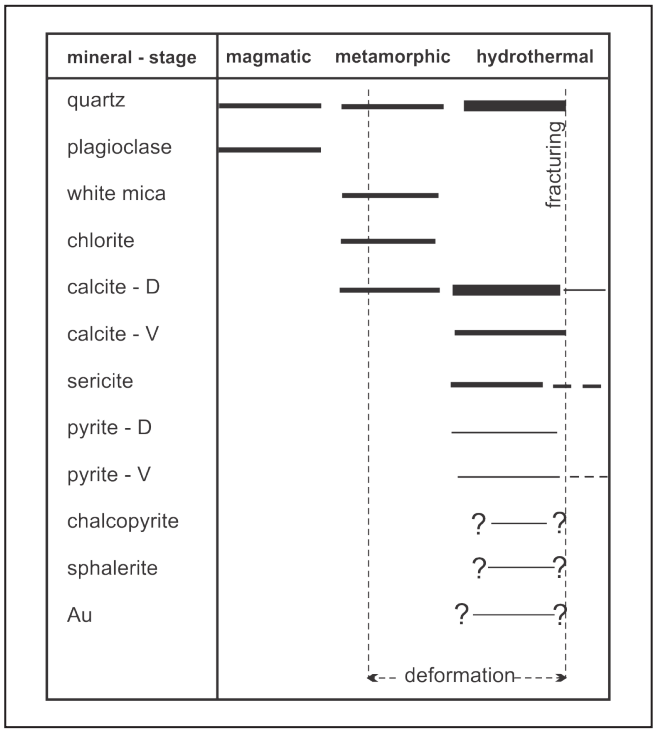

FIGURE 5. Schematic paragenetic sequences in distinct stages of the host rocks and hydrothermal alteration in the Enche Concha and Tunel prospects. The thickness of the lines indicates the importance of the different stages.

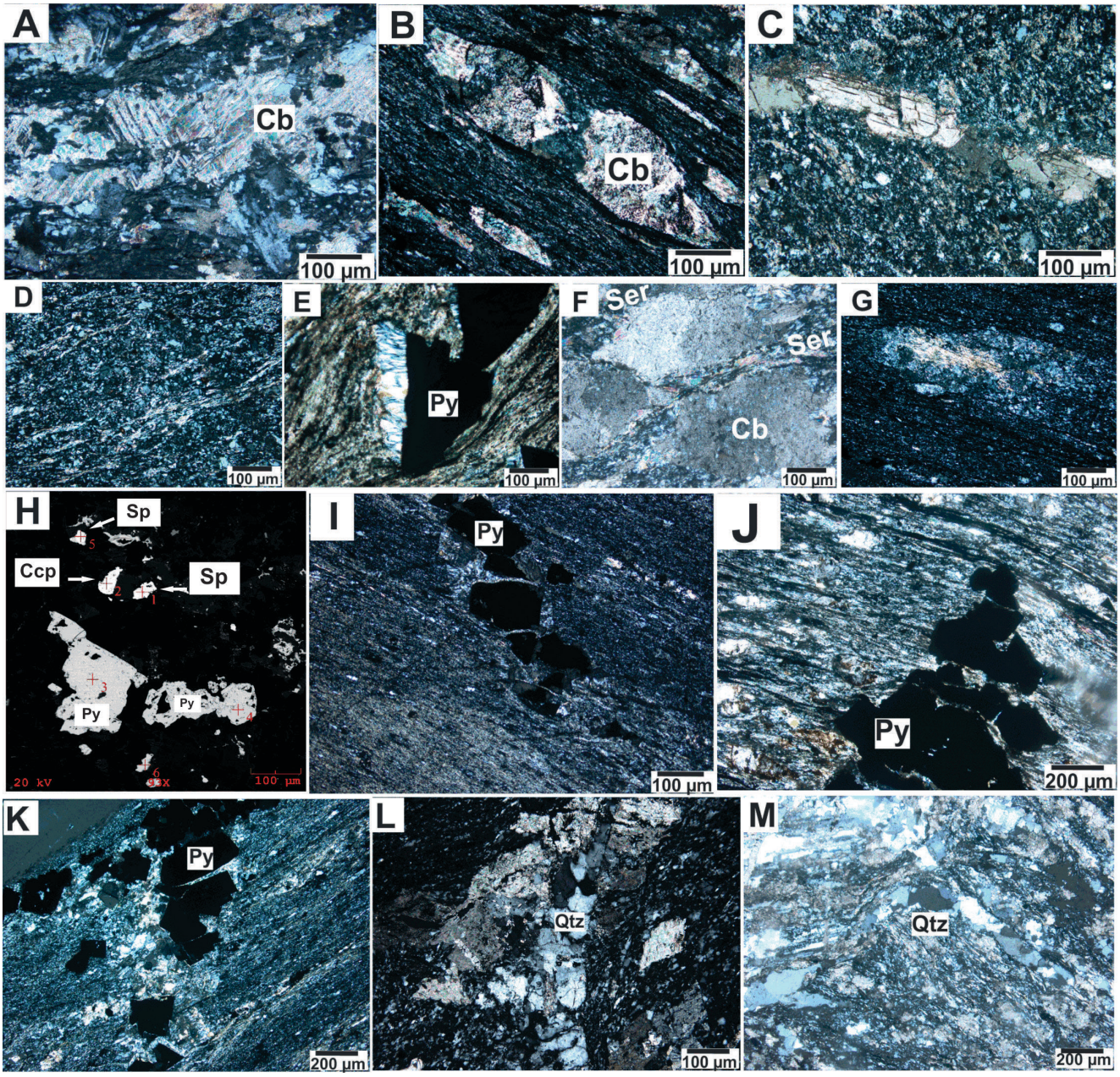

FIGURE 6. Microscopic images of the hydrothermal alteration. (A) Plagioclase crystal replaced by carbonate. (B) Plagioclase porphyroclast replaced by carbonate. (C) Carbonate veinlet cutting dacite. (D) Sericite alteration defining the foliation in dacite. (E) Sericite crystallized in pressure shadow of pyrite and along the foliation in phyllite. (F) Fracture-filling sericite cutting carbonate crystal. (G) Sericitized plagioclase. (H) Scanning microscope image of subhedral to anhedral pyrite grains in association with sphalerite and chalcopyrite. The crosses identify the locus of Energy Dispersive Spectroscopy analysis with gold grades ranging from 0.86 to 3.6 wt.%. (I) Subhedral pyrite grains and associated sericitic alteration in phyllite. (J) Anhedral pyrite grains discordant to the foliation of phyllite. (K) Quartz-carbonate-sulfide veinlet discordant to the foliation of phyllite. (L) Quartz veinlet cutting carbonatized phyllite. (M) Folded quartz veinlet. Mineral abbreviations: Cb – carbonate, Ccp – chalcopyrite, Py – pyrite, Qtz – quartz, Ser – sericite. All images (except H) were obtained with crossed nicols.

These veins are mm- to a few cm-thick and are in general discordant to the foliation, but show deformation features, such as micro-folding and subgrain generation (Figs. 6L, 6M). The occurrence of thicker (up to 30 cm-thick), massive to laminated gold-bearing quartz veins, which have been mined by artisanal miners (indicating the presence of free-milling gold), has been informed by unpublished company report (Kinross).

Free gold particles have not been observed in our investigation. Gold was detected by scanning electron microscopy, ranging in grade mostly from 0.83 to 1.57%, but reaching higher grades (5-6%) in deformed pyrite crystals present in quartz veins.

5. Fluid Inclusions

The fluid inclusion study was carried out on quartz crystals from sulfide-bearing (mineralized) veins from the Tunel prospect, sampled from drill core JB08 at the depths of 73.2 and 74.5 m (Fig. 7A). Over 180 fluid inclusions have been analyzed microthermometrically.

5.1. Types and distribution

The quartz crystals that host fluid inclusions are anhedral, with irregular rims, and often forming subgrains (Fig. 7B).

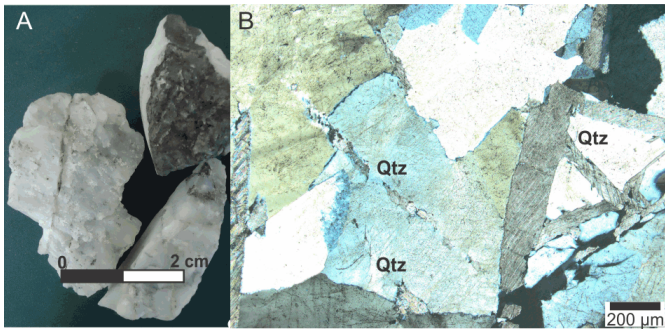

FIGURE 7. (A) Sample of quartz-sulfide vein used for fluid inclusion study. (B) Photomicrography, on crossed nicols, of the quartz vein showing the characteristics of the quartz grains.

The fluid inclusions occur in clusters, in isolation, or in trails (Fig. 8). Necking down features are common in larger inclusions (>5 μm) from all types. These necked inclusions were not included in microthermometric studies. Microscopic investigation at room (22-24°C) and sub-zero temperatures allowed the identification of three types of fluid inclusions. One type is comprised of one-phase inclusions that did not show phase transitions during the microthermometric work. These monophasic inclusions are probably metastable or empty cavities and will not be further addressed in this paper.

The Type-1 consist of aqueous-carbonic fluid inclusions having two phases. These phases comprise liquid water plus liquid CO_2, or liquid water and gaseous CO_2 (Fig. B). The type-2 consists of aqueous fluid inclusions and is formed predominantly by two-phase (liquid + vapor) and subordinately one-phase (liquid) inclusions (Figs. 8C, 8D).

Type-1 fluid inclusions are less abundant than Type-2 and occur predominantly as isolated individuals, and subordinately in clusters (primary inclusions) and trails (secondary inclusions). The morphology is rounded to ellipsoidal, and they vary in size between 3 and 5 μm. The carbonic phase occupies 15 to 30% of the inclusion cavities.

The more abundant Type-2 occurs as clusters and intragranular trails, and rarely in isolation. These inclusions are primary and pseudo-secondary in origin, and are rounded or polygonal, with sizes ranging from 2 to 5 μm. The vapor phase occupies 80% of the inclusion cavities, but some inclusions have 70 to 60% of the vapor phase.

When in clusters, Type-1 and 2 inclusions occur as an association, and no temporal (crosscutting) relationships could be established, suggesting that the two types were trapped at the same time and belong to a single Fluid Inclusion Assemblage (FIA – Goldstein and Reynolds 1994).

5.2. Microthermometric results

The following abbreviations are used in text and figures. $TmCO_2$: temperature of melting of the carbonic phase, $ThCO_2$: temperature of homogenization of the carbonic

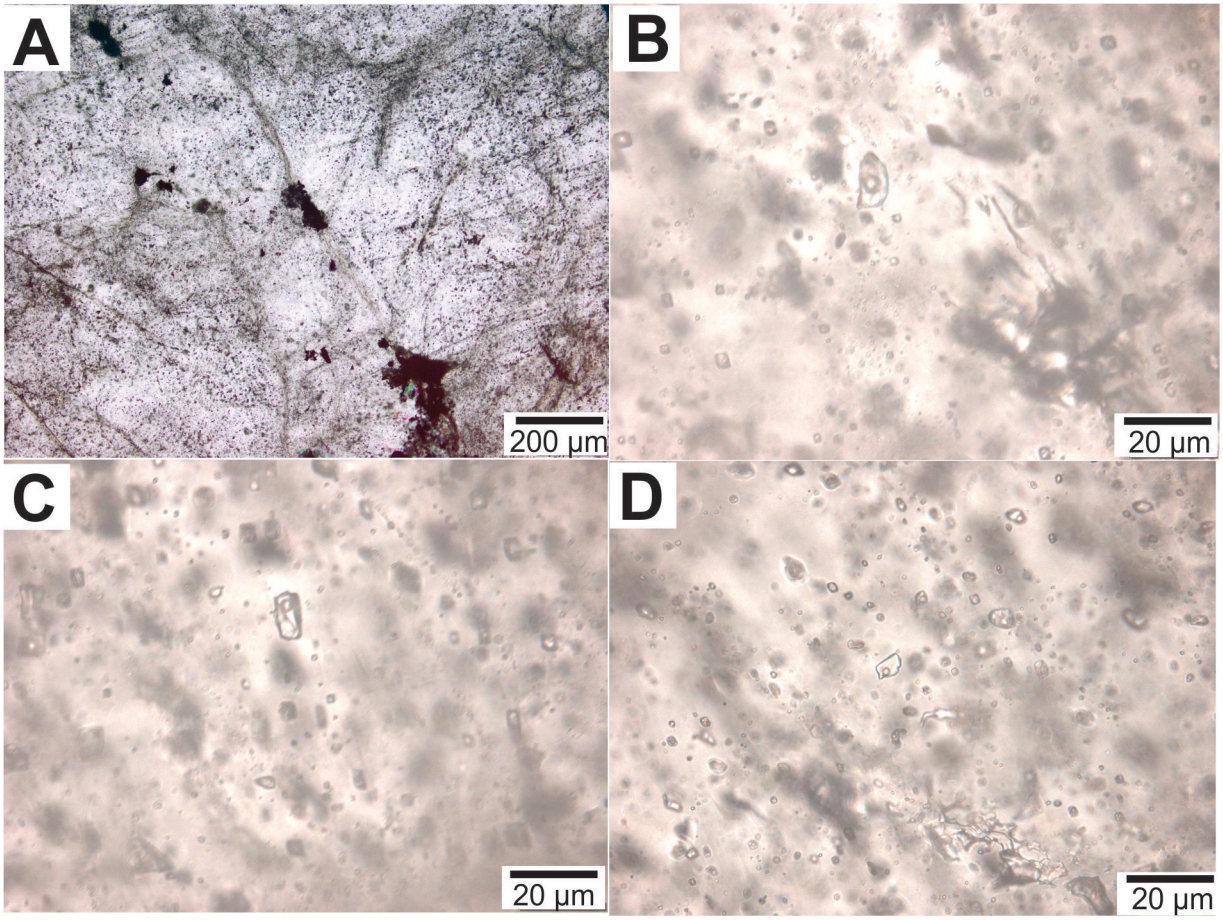

FIGURE 8. Photomicrographs showing types and distribution of the fluid inclusions. (A) General view of a quartz grain with trails of fluid inclusions. (B) Large two-phase aqueous-carbonic (Type-1) fluid inclusion occurring in the same microscopic domain with Type-2 aqueous inclusions. (C) Large two-phase aqueous inclusion in spatial association with one-phase inclusions. (D) Cluster and trails of Type-2 inclusions.

phase, Tmclat: clathrate melting temperature, Tmice: final ice melting temperature, Teu: eutectic melting temperature, Tht: temperature of final/total homogenization. Considering the state of homogenization, L stands for liquid, and V for vapor.

Type-1 aqueous-carbonic fluid inclusions show $TmCO_2$ values ranging from -56.6 and -57.3°C (Fig. 9A). The $ThCO_2$ in the same type varies between 12 and 25.6°C (Fig. 9B), mostly to the liquid state, whereas Tmclat is in the range of 6.0 to 8.4°C (Fig. 9C). The Tht ranges from 251 to 370°C (Fig. 9D).

In the two-phase Type-2 fluid inclusions, only a few Teu have been observed, ranging from -24.5 to -20.0°C, and Tmice varies between -0.1 and -4.1°C (Fig. 9E). Tht is in the range of 167 and 342°C (Fig. 9D).

5.3. Density and composition

Density and compositional data were calculated based on the microthermometric results. The global and CO_2 densities of the aqueous-carbonic fluid inclusions vary from 0.7 to 1.0 g/cm^3, and 0.2 to 1.0 g/cm^3, respectively (Bowers and Helgeson 1983). The salinity of these fluid inclusions are in the range of 4.4 to 5.3 wt.% NaCl equivalent (based on Collins 1979), and the small variation in the $TmCO_2$ values in relation to the pure CO_2 values, indicates only minor amounts (up to 5%) of additional components, such as N_2 and/or CH_4 in the carbonic phase (e.g., Van den Kerkhof and Thiéry 2001). The estimated XCO_2 values range from 0.03 to 0.13. For the aqueous inclusions, densities of 0.7 to 0.9 g/cm^3, and salinities of 0.2 to 6.3 wt.% NaCl equivalent are estimated according to Brown and Lamb (1986).

5.4 Origin of the fluid inclusions

Petrographic and microthermometric results have shown that the two types of fluid inclusions occur in association in the same microscopic domains of the hosting quartz, and that the two types homogenized broadly in the same range of temperatures (Figs. 9D, 10, and 11). These features suggest that the two types are coeval and belong to a single system. A few aqueous fluid inclusions with Tht of 300-350°C have lower salinities (1-2%) when compared with the majority of the inclusions (3-6%) (Fig. 9C). We don't have a clear answer to this fact, which might be attributed to local conditions of trapping of more diluted fluid.

The contemporaneous trapping together with the variation in Tht in a single domain (Fig. 10) is indicative of phase separation (e.g., Wilkinson 2001), which may be triggered by different processes, such as pressure fluctuation (Robert et al. 1995), as observed in the range of estimated pressures, and CO_2 removal due to carbonate crystallization (Rimstidt 1997). These are common features identified in the other orogenic gold deposits of the Gurupi Belt (e.g., Klein 2014).

6. Isotope geology

6.1. Stable isotopes

The stable isotope compositions were measured in hydrothermal minerals and fluids: oxygen in vein quartz; oxygen, and carbon in vein and disseminated calcite from the carbonate alteration; hydrogen in inclusion fluids hosted in quartz (Table 1).

The $\delta^{18}O$ values of quartz from Enche Concha vary between +16.6 and +16.9‰ in mineralized veins and is +17.7‰ in a barren quartz vein, whereas mineralized samples from Tunel range from +15.3 to +16.3‰. The δD values of inclusion fluids from two mineralized samples are -28 and -25‰ in the Enche Concha and Tunel prospects, respectively.

The $\delta^{13}C$ values of calcite vary between -10.6 and -11.4‰ in the disseminated type, and is -9.8‰ in the quartz-calcite-sulfide vein from Enche Concha. In the same prospect, the $\delta^{18}O$ values are in the range of +14.3 to +16.1‰ for the disseminated variety, and is +14.5‰ for the vein calcite. In the Tunel prospect, the $\delta^{13}C$ and $\delta^{18}O$ values range from -14.1 to -15.1‰, and +14.8 to +16.2‰, respectively. As a whole, the oxygen compositions are similar, but the $\delta^{13}C$ values are quite lower in the Tunel samples.

6.2. Sr isotopes

The isotope composition of Sr was measured in hydrothermal calcite from the disseminated carbonate alteration (Table 2). Irrespective of the host rock type (phyllite or dacite), the obtained 87Sr/86Sr ratios are weakly radiogenic and range from 0.702699 to 0.705141 for the Enche Concha samples, and from 0.703055 to 0.705080 at Tunel. Therefore, no difference exists in the Sr isotopic composition in the two prospects.

7. Discussions

7.1. Physico-chemical conditions of mineralization (T-P-fO_2-pH)

The estimated temperature and pressure conditions of gold mineralization is based on the microthermometric results from fluid inclusions and isotope thermometry. The oxygen isotope compositions of the coexisting quartz-calcite pair from sample JB04_238.6 yielded a temperature of 328°C using the equation of Sharp and Kirchner (1994). This value is in line with the interval of total homogenization temperatures measured in the aqueous-carbonic fluid inclusions (~260-370°C).

For pressure estimations, we used the above temperature data, along with salinity, CO_2 density, and isochores calculated according to Bowers and Helgeson (1983) for the system CO_2-H_2O-NaCl. These data yielded a pressure range of 0.85 to 2.8 kbar (Fig. 12A), implying 3 to 9 km in depth, assuming lithostatic conditions, which is compatible with the structural setting of mineralization.

For the calculated T-P-XCO_2 range, a log fO_2 value of -32.1 is estimated for the oxygen fugacity of the fluid using the method of Huizenga (2005). This value lies above the CO_2-CH_4 buffer (Fig. 12B), which is in line with the fluid inclusion $TmCO_2$ data, and indicates relatively reduced conditions during gold mineralization. Additionally, the presence of calcite and sericite in the hydrothermal alteration, together with the lack of K-feldspar, indicates a solution with near neutral to slightly alkaline pH (ca. 5.0 to 6.2; Romberger 1990; Hayashi and Ohmoto 1991).

7.2. Fluid composition and potential sources

The composition of the hydrothermal fluid was estimated from the stable isotope results, using relevant fractionation factors and temperature (328°C), and from direct measuring of the isotopic composition of fluid inclusions (Table 1). The

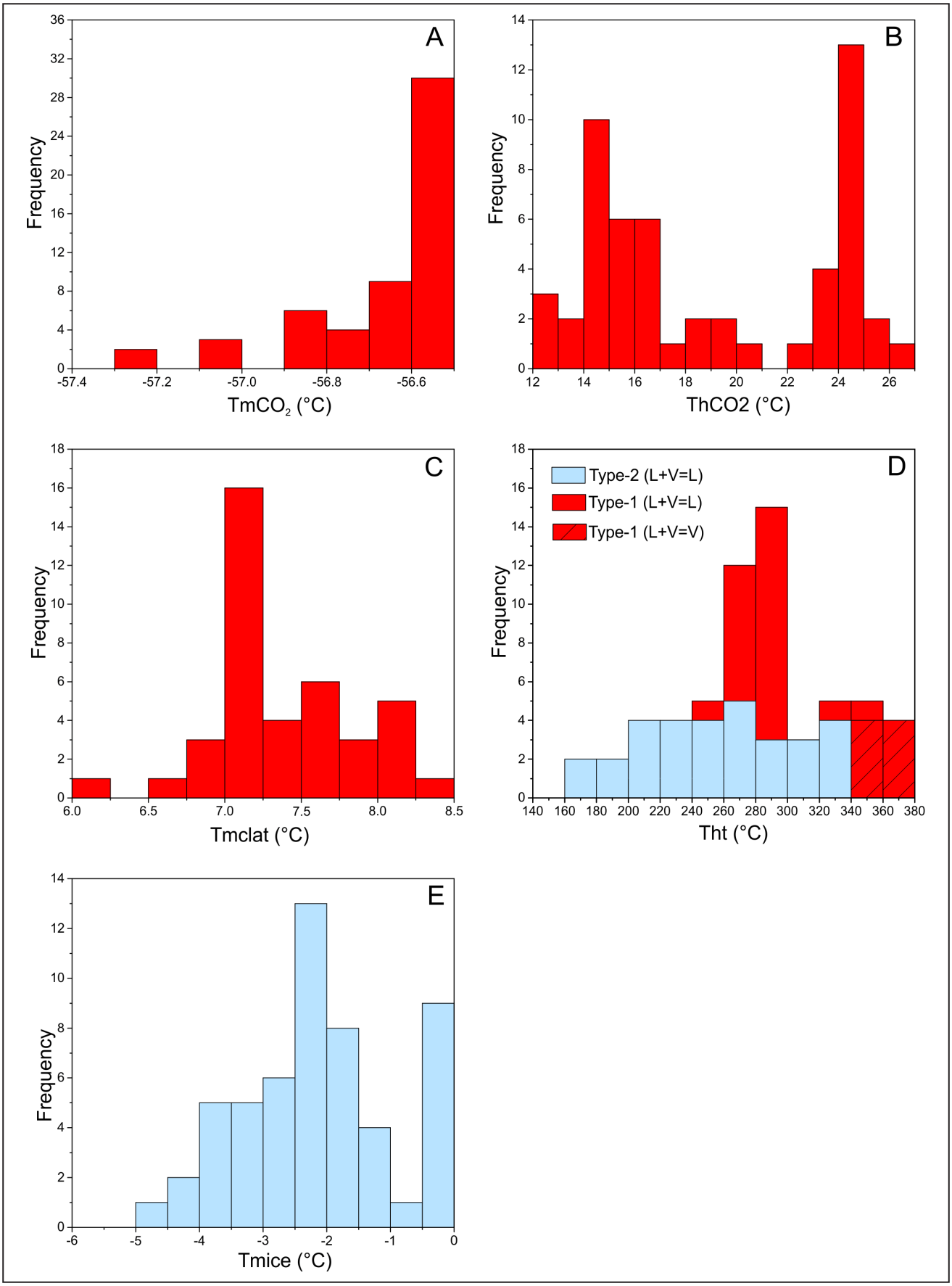

FIGURE 9. Histograms of the microthermometric results. (A) Temperature of CO_2 melting from Type-1 fluid inclusions. (B) Temperature of CO_2 homogenization from Type-1 fluid inclusions. (C) Temperature of clathrate melting in Type-1 fluid inclusions. (D) Total homogenization temperature for Type-1 and Type 2 fluid inclusions (V: vapor, L: liquid). (E) Final ice melting temperature for Type-2 fluid inclusions

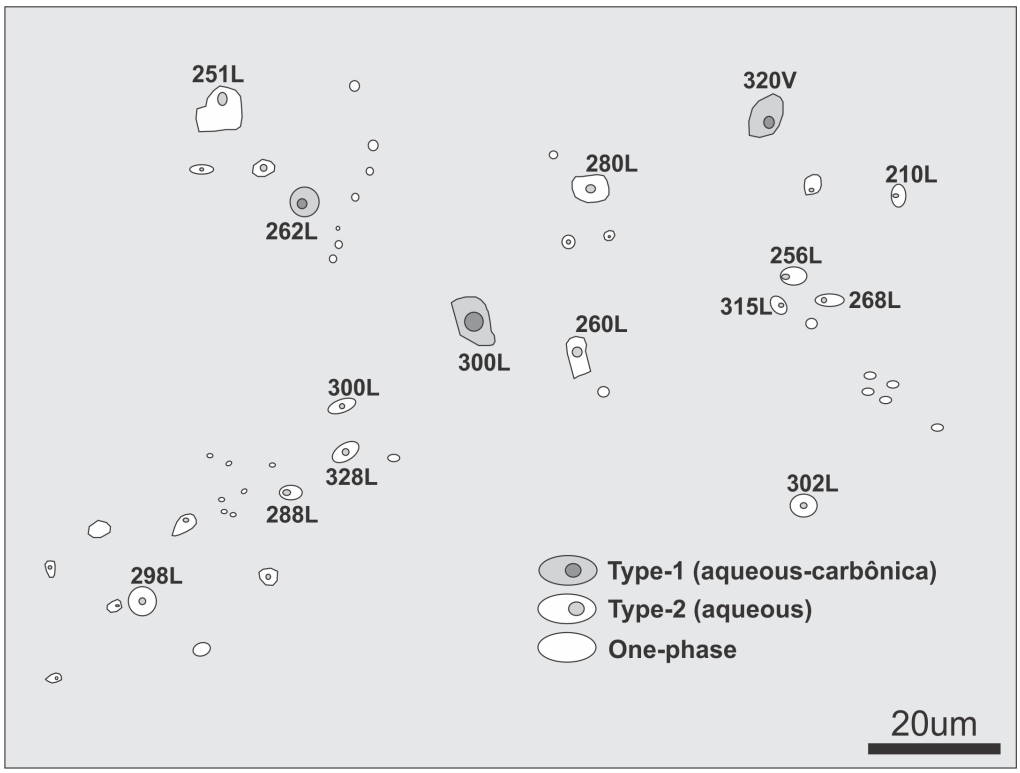

FIGURE 10. Hand sketch showing the distribution and textural relationships between different types of fluid inclusions in a single microscopic domain (sample JB08_74.5). The numbers near the inclusions indicate the final homogenization temperature (L: liquid, V: vapor). Photographs obtained at room temperature (22-24°C).

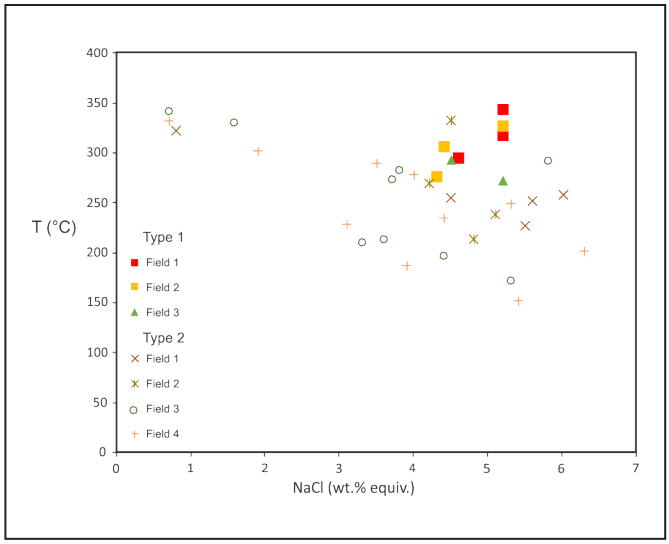

FIGURE 11. Final homogenization temperature versus salinity plot for Type-1 and Type-2 fluid inclusions. Each symbol represents the average values for a single Fluid Inclusion Assemblage.

calculated and measured fluid compositions, along with the Sr isotope and fluid inclusion results, were then compared to those of potential sources.

The $\delta^{18}O$ values of the water in equilibrium with quartz is +10.7 to +11.0‰ at Enche Concha, and +9.4 to +10.4‰ at Tunel (quartz-H_2O fractionation factor of Matsuhisa et al. 1979). Calculated for calcite the fluid $\delta^{18}O$ values are in the range of +9.5 to 11.3‰ for the disseminated calcite, and is + 9.7‰ for the vein calcite in the Enche Concha prospect. At Tunel, the values are +10.0 and +11.4‰ (calcite-H_2O fractionation factor of Friedman and O'Neil 1977). As a whole, the fluid $\delta^{18}O$ values have similar ranges in quartz and calcite from the two prospects (+9.4 to +11.4‰). These values, in combination with the δD values from inclusion fluids suggest a metamorphic source for the fluid (Fig. 13A).

The $\delta^{13}C$ values of the CO_2 in equilibrium with calcite (calcite-CO_2 fractionation factor of Ohmoto and Rye 1979) range from -8.3 to -9.1‰ for the disseminated stage, and is -7.6‰ for the vein calcite at Enche Concha. The values for Tunel are -11.8 and -12.8%. Theses CO_2 $\delta^{13}C$ values are not diagnostic of a specific carbon source. Instead, the variation in the isotopic composition might indicate variable contribution of organic carbon from the carbonaceous schists and phyllites of the hosting Chega Tudo Formation, which is a common feature in the Gurupi Belt (e.g., Klein et al., 2005). In addition, the fluid $\delta^{13}C$ value of the quartz-carbonate-sulfide is the highest among the studies samples (Fig. 13B), and this composition may be closer to that of the mineralizing fluid, indicating a deep seated source (Ohmoto and Rye 1979).

In closed systems, minerals with insignificant contents of Rb, such as calcite, which does not incorporate this element in its structure, preserve the initial $^{87}Sr/^{86}Sr$ ratio (Mueller et al. 1991). In consequence, the $^{87}Sr/^{86}Sr$ ratios of hydrothermal calcite may be used as an approximation to the Sr isotope composition of hydrothermal fluids, and in the investigation of changes that the fluids may undergo by interaction with regional rocks or with mineralized host rocks (Kontak and Kerrich 1995; Scanlan et al. 2018). Furthermore, even for carbonates that have recrystallized or re-equilibrated at low temperatures, the Sr and C isotopic systems are sufficiently resistant to preserve the original compositions (Kerrich 1987). The relatively low 87Sr/86Sr ratios

TABLE 1 – Stable isotope (C, O, H) compositions of hydrothermal minerals and inclusion fluids.

Target	Sample	Mineral	Stage	$\delta^{18}O$ (‰)	$\delta^{13}C$ (‰)	δD (FI) (‰)
Enche Concha	JB02_74	Quartz	Vein (barren)	+17.7		
	JB02_100.9	Calcite	Dissemination	+14.3	-10.6	
	JB02_140	Calcite	Dissemination	+16.1	-11.1	
	JB02_149.5	Calcite	Dissemination	+15.5	-11.4	
	JB04_238.6	Quartz	Vein	+16.9		
	JB04_238.6	Calcite	Vein (qtz-cc-sulf)	+14.5	-9.8	
	JB04_261	Quartz	Vein	+16.6		-28
Tunel	JB08_51	Quartz	Vein	+16.0		
	JB08_51	Calcite	Dissemination	+14.8	-14.1	
	JB08_73	Quartz	Vein	+16.3		
	JB08_75	Quartz	Vein	+15.3		-25
	JB08_96.15	Calcite	Dissemination	+16.2	-15.1	

FI: fluid inclusion water, qtz: quartz, cc: calcite, sulf: sulfide

TABLE 2 – Strontium isotope compositions of hydrothermal calcite from the disseminated carbonate alteration.

Target	Sample	Host rock	$^{86}Sr/^{88}Sr$	2σ	$^{87}Sr/^{86}Sr$	2σ	$^{84}Sr/^{88}Sr$	2σ
Enche Concha	JB02_100.9	Phyllite	0.119183	0.000057	0.705141	0.000027	0.006739	0.000006
	JB02_149.5	Phyllite	0.117123	0.000052	0.702699	0.000028	0.006739	0.000006
	JB04_165	Phyllite	0.118589	0.000225	0.703110	0.000021	0.006739	0.000002
Tunel	JB08_51	Dacite	0.117549	0.000077	0.703160	0.000034	0.006739	0.000018
	JB08_56.8	Phyllite	0.118769	0.000058	0.703055	0.000028	0.006739	0.000002
	JB08_96.15	Dacite	0.119411	0.000114	0.705080	0.000025	0.006739	0.000004

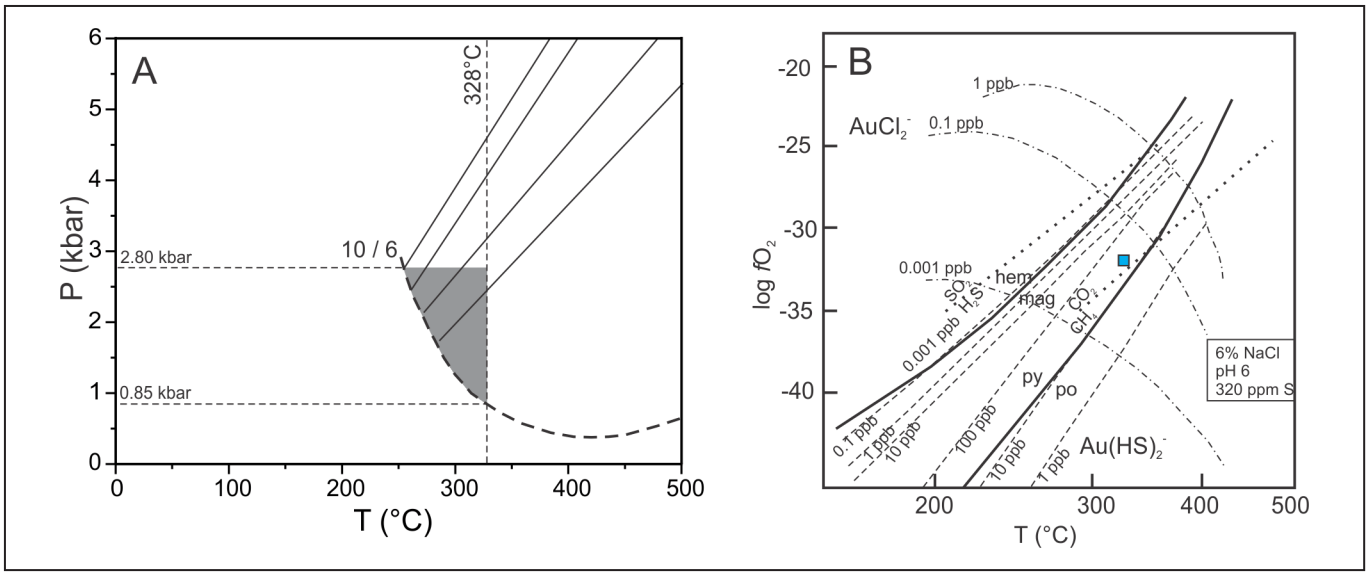

FIGURE 12. Physico-chemical diagrams for the Enche Concha and Tunel prospects. (A) P-T plot showing the estimated conditions for gold mineralization (shaded box), using the isochores calculated to the range of XCO_2 of the aqueous-carbonic fluid inclusions. The vertical dashed line stands for the temperature obtained with the oxygen isotope thermometry, whereas the thick dashed line is the solvus for the CO_2-H_2O-NaCl system for 10 mol% CO_2 and 6 wt% NaCl equiv. (from Bowers and Helgeson 1983). (B) Aqueous solubility of gold as a function of temperature and oxygen fugacity. The dotted-dashed lines are for the chloride complex [$AuCl_2$-], whereas the dashed lines are for the bisulfide complex [$Au(HS)_2$-]. The thick solid lines represent the limits of the stability fields of sulfides and iron oxides, and the dotted lines stand for other buffers (adapted from Romberger 1990, and Ohmoto and Goldhaber 1997).

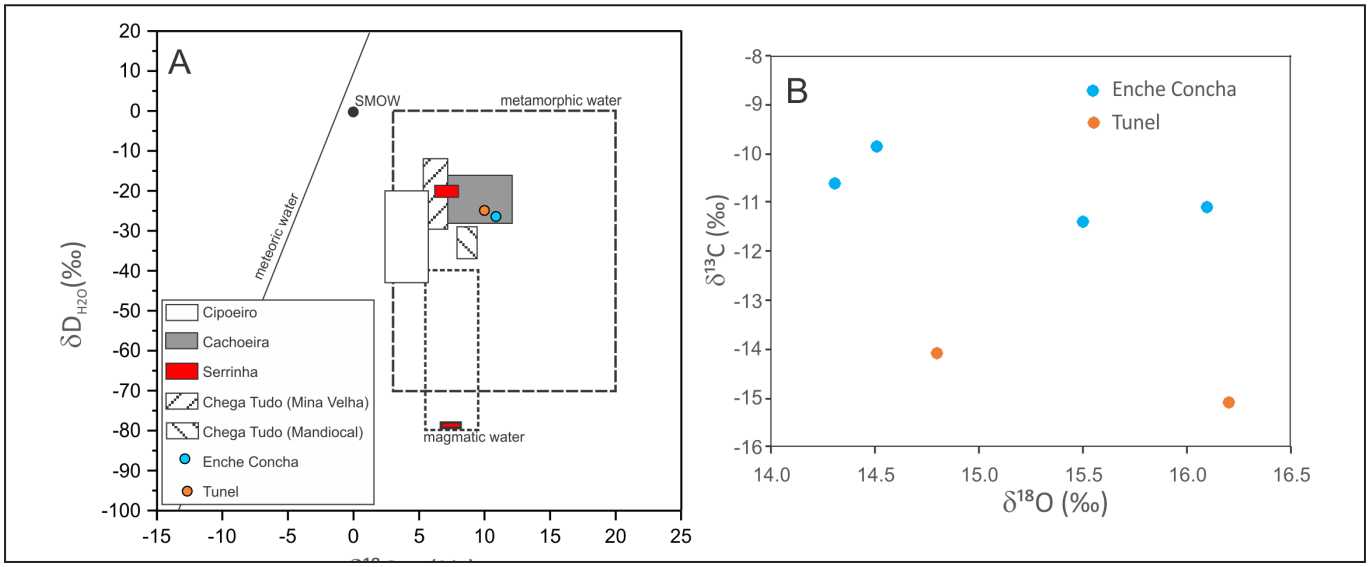

FIGURE 13. (A) Oxygen and hydrogen isotopic composition of the hydrothermal fluids at Enche Concha and Tunel compared with available data for orogenic gold deposits of the Gurupi Belt (Klein 2014). The fields for magmatic and metamorphic waters are from Sheppard (1986) and the meteoric water line is from Craig (1961). SMOW = Standard Mean Ocean Water. (B) Carbon and oxygen isotopic composition of hydrothermal calcite.

(~0.7027-0.7051) measured in the hydrothermal calcite from Enche Concha and Tunel indicate a little evolved source with low Rb/Sr ratio. Comparing with the composition of orogenic gold deposits from different cratons and ages, we can observe that our results are lower than those of the orogenic deposits (Fig. 14). Our results are also lower than those presented by the regional Rhyacian rocks of the Gurupi Belt and adjoining São Luís cratonic fragment (Fig. 14). This indicates that the Sr present in the mineralizing fluid is externally-derived and that the regional rocks have not contributed with Sr to the fluid. Furthermore, the data indicate a probable deep source for Sr, such as the lower crust or mantle (Fig. 14).

7.3. Genetic constraints

Some interpretations about the genesis of the gold mineralization can be drawn for the studied prospects, based on the fluid inclusion and isotopic data. The physico-chemical characteristics of the fluid, the presence of pyrite as the main sulfide mineral, and the lack of significant amounts of base metals suggest the H_2S (alternatively HS-) as the main sulfur species in the fluid. This, together with the oxygen fugacity estimation indicate $Au(HS)_2$- as the gold transporting complex (Fig. 12B). The destabilization of this complex and deposition of gold from solution might be ascribed to phase separation,

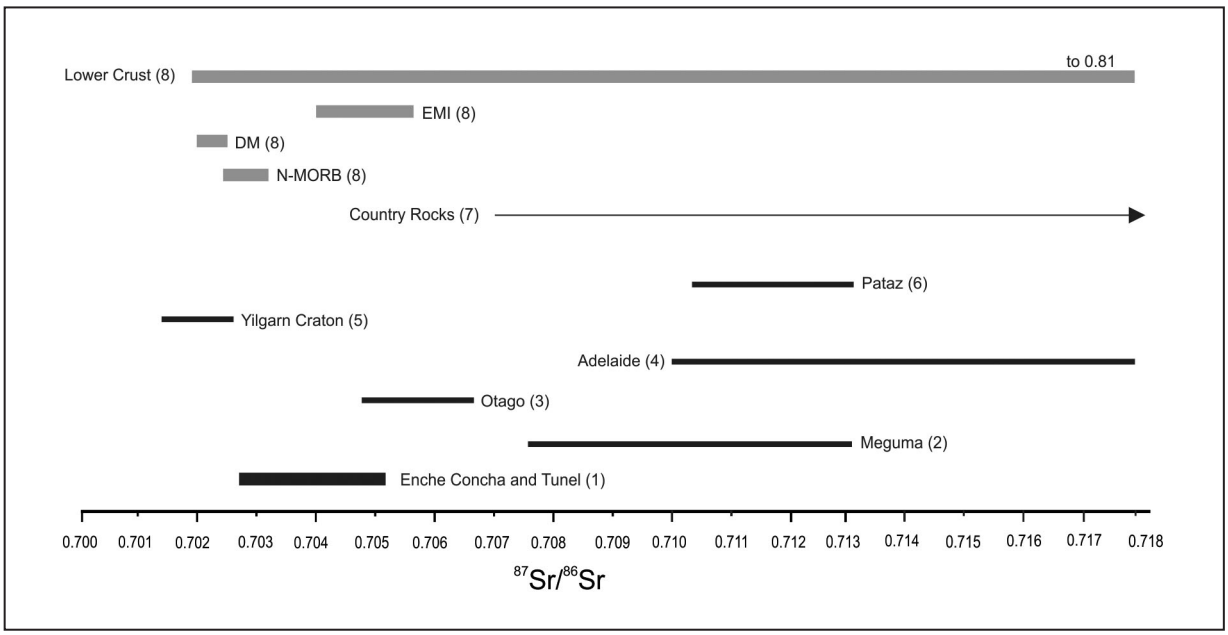

FIGURE 14. Strontium isotope composition of hydrothermal calcite from Enche Concha and Tunel compared to the isotopic compositions of orogenic gold deposits worldwide, and with potential sources. References: (1) this study, (2) Kontak and Kerrich (1995), (3) Scanlan et al. (2018), (4) Griessmann (2011), (5) Mueller et al. (1991), (6) Haeberlin (2002), (7) Rhyacian granitoids and gneisses of the Gurupi Belt and São Luís cratonic fragment, compiled from Hurley et al. (1968) and Klein and Moura (2003) and recalculated to the crystallization age, (8) large terrestrial reservoirs, compiled from Rollinson (1993). DM: depleted mantle, EMI: enriched mantle, N-MORB: normal mid ocean ridge basalts.

as documented by the fluid inclusion study, along with fluid-rock interactions, which is inferred from the carbon isotope data (reaction with organic carbon) and from the refractory character of gold, which is present in the structure of pyrite. Changes in the pH of the fluid by sericitization and removal of CO_2 of the fluid to produce calcite might have also contributed to the breakdown of the sulfur complex.

Our results and interpretations are similar to those described for other gold deposits in the Gurupi Belt (Klein 2014) and elsewhere, being consistent with the orogenic gold system (e.g., Goldfarb and Groves 2015, and references therein).

8. Conclusions

The Enche Concha and Tunel exploration targets (prospects) have gold mineralization hosted in dacites and phyllites that belong to the ca. 2160 Ma-old metavolcano-sedimentary Chega Tudo Formation. Petrographic, fluid inclusion, and isotopic (O, H, C, Sr) data allowed the following observations and conclusions to be drawn.

(1) The hydrothermal alteration comprises the formation of pervasive and fissure-filling carbonate, sericite, and sulfides (pyrite and subordinate chalcopyrite and sphalerite), in addition to quartz (±carbonate, ±sulfides). Refractory gold occurs in pyrite.

(2) The alteration and mineralization are associated with previously defined Paleoproterozoic deformation phase.

(3) The hydrothermal alteration and gold mineralization occurred between 260 and 370°C, from 0.85 to 2.8 kbar, from an aqueous-carbonic, relatively reduced and near neutral metamorphic fluid, with contributions from deep-seated (lower crust and mantle) sources.

(4) Gold was transported by a sulfur-bearing complex and precipitation occurred in response to phase separation and fluid-rock interactions.

(5) The geological and genetic characteristics are equivalent to those of the orogenic gold system previously defined for the Gurupi Belt.

Acknowledgements

The authors acknowledge IAMGOLD for the access to the project area and to drill cores. The Brazilian funding agency CNPq (Conselho Nacional de Desenvolvimento Científico e Tecnológico) is thanked for the scholarship to RFMJr and for research grants to ELK (306798/2016-6) and JML (307199/2015-0). Dr. Regis Borges (UFPA) is thanked for suggestions on an early version of this work. We thank the JGSB reviewers, Dr. Valmir Souza (UnB) and Dr. Lucilia Oliveira (CDTN) for their comments, which help us to improve the final version of the manuscript.

References

Bowers T.S., Helgeson H.C. 1983. Calculation of the thermodynamic and geochemical consequences of non-ideal mixing in the system H_2O-CO_2-NaCl on phase relations in geological systems: equation of state for H_2O-CO_2-NaCl fluids at high pressures and temperatures. Geochimica et Cosmochimica Acta, 47, 1247–1275.

Brown P.E. 1989. Flincor: a microcomputer program for the reduction and investigation of fluid-inclusion data. American Mineralogist, 74, 1390-1393.

Brown P.E., Lamb W.M. 1986. Mixing of H2O e CO2 in fluid inclusions. Geobarometry and Archean gold deposits. Geochimica et Cosmochimica Acta, 50, 847-852.

Collins P.L.F. 1979. Gas hydrates in CO2-bearing fluid inclusions and the use of freezing data for estimation of salinity. Economic Geology, 74, 1435-1444.

Craig, H. 1961. Isotopic Variations in Meteoric Waters. Science, 133, 1702-1703.

Friedman I., O'Neil, J.R. 1977. Compilation of stable isotope fractionation factors of geochemical interest. U.S. Geology Survey Bulletin, 440 (KK): 1-12.

Goldfarb, R.J., Groves D.I. 2015.Orogenic gold: Common or evolving fluid and metal sources through time. Lithos 233, 2-26.

Goldstein R.H., Reynolds T.J. 1994. Systematics of fluid inclusions in diagenetic minerals. SEPM Short Course 31, 199.

Griessmann, M. 2011. Gold mineralization in the Adelaide fold belt. PhD Thesis. The University of Adelaide, 331 p.

Haeberlin Y. 2002. Geological and Structural Setting, Age and Geochemistry of the Orogenic Gold Deposits at the Pataz Province, Eastern Andean Cordillera, Peru. PhD Thesis, Université de Genève, 182 p.

Harris, C., Vogeli, J. 2010. Oxygen isotope composition of garnet in the Peninsula Granite, Cape Granite Suite, South Africa: constraints on melting and emplacement mechanisms. South African Journal of Geology 113, 401-412.

Hayashi K.I., Ohmoto H. 1991. Solubility of gold in NaCl- and H2S-bearing aqueous solutions at 250-350°C. Geochimica et Cosmochimica Acta 55, 2111-2126.

Huizenga, J.M. 2005. COH, an Excel spreadsheet for composition calculations in the C–O–H fluid system. Computers & Geosciences 31, 797-800.

Hurley, P.M., Melcher, G.C., Pinson, W.H., Fairbairn, H.W. 1968. Some orogenic episodes in South America by K–Ar and whole-rock Rb–Sr dating. Canadian Journal of Earth Sciences 5, 633–638.

Kerrich R. 1987. The stable isotope geochemistry of Au-Ag in deposits in metamorphic rocks. In: Kyser, T.K. (Ed.), Stable isotope geochemistry of low temperature fluids. Mineralogical Association of Canada, p. 287-336. (Short Course, v. 13).

Klein E. L. 2014. Ore fluids of orogenic gold deposits of the Gurupi Belt, Brazil: a review of the physico-chemical properties, sources, and mechanisms of Au transport and deposition. Geological Society, London, Special Publications. https://doi.org/10.1144/SP402.2

Klein E.L., Moura C.A.V. 2003. Síntese geológica e geocronológica do Craton São Luíse do Cinturão Gurupi na região do rio Gurupi (NE-Para/NW-Maranhão). Revista Geologia USP, Série Científica 3, 97-112.

Klein, E.L., Harris, C., Giret, A., Moura, C.A.V., Angélica, R.S. 2005. Geology and stable isotope (O, H, C, S) constraints on the genesis of the Cachoeira gold deposit, Gurupi belt, northern Brazil. Chemical Geology, 221, 188–206.

Klein, E.L., Lopes, E.C.S., Rodrigues, J.B., Souza-Gaia, S.M., Cordani, U.G. 2020. Rhyacian and Neoproterozoic magmatic associations of the Gurupi Belt, Brazil: Implications for the tectonic evolution, and regional correlations. Geoscience Frontiers https://doi.org/10.1016/j.gsf.2020.02.016

Kontak D., Kerrich R. 1995. Geological and geochemical studies of a metaturbidite-hosted lode gold deposit: the Beaver Dam deposit Nova Scotia: II. isotopic studies. Economic Geology, 90, 885-901.

Matsuhisa Y., Goldschmit J.R., Clayton R.N. 1979. Oxygen isotope fractionation in the system quartz-albite-anorthite-water. Geochimica et Cosmochimica Acta.,43: 1131-1140.

Mueller A.G., De Laeter, J.R., Groves D.I. 1991. Strontium isotope systematics of hydrothermal minerals from epigenetic Archean gold deposits in the Yilgarn Block, Western Australia. Economic Geology, 86, 780-809.

Ohmoto H., Rye R.O. 1979. Isotopes of sulfur and carbon. In: BarnesHL (Ed,) Geochemistry of hydrothermal ore deposits. Wiley, New York, pp 509–567.

Ohmoto H., Goldhaber, M.B. 1997, Sulfur and carbon isotopes, in Barnes H.L.(Ed.), Geochemistry of hydrothermal ore deposits: John Wiley, p. 517–611.

Rimstidt J. D. 1997. Quartz solubility at low temperatures. Geochimica et Cosmochimica Acta, 61: 2553-2558.

Robert F., Boullier A.M., Firdaous K. 1995. Gold-quartz veins in metamorphic terranes and their bearing on the role of fluids in faulting. Journal of Geophysical Research 100 (B7), 12861-12879.

Roedder E. 1984. Fluid Inclusions. Mineralogical Society of America. Reviews in Mineralogy. 12, 644 p.

Rollinson H. R., 1993. Using geochemical data: evaluation, presentation, interpretation. London: Longman Scientific & Technical, 352 p.

Romberger S. B. 1990. Geochemistry of epithermal precious metal deposits. Gold'90, Proceedings of the Gold'90 Symposium, Littleton, Colorado, USA, p. 181-188.

Scanlan E.J., Scott J.M., Wilson V.J., Stirling C.H., Reid M.R., Le Roux P.J. 2018. In situ87Sr/86Sr of scheelite and calcite reveals proximal and distal fluid-rock interaction during orogenic W-Au mineralization, Otago Schist, New Zealand. Economic Geology, 113, 1571-1586.

Sharp Z. D., Kirschner D. L. 1994. Quartz–calcite oxygen isotope thermometry: A calibration based on natural isotopic variations. Geochimica et Cosmochimica Acta, 58, 4491-4501.

Shepherd T.J., Rankin A.H., Alderton D.H. 1985. A practical guide to fluid inclusions studies: Glasgow, Blackie and Son. 239p.

Sheppard S.M.F. 1986. Characterization and isotopic variations in natural waters. In: Valley J.W., Taylor Jr H.P., O'Neil J.R. (Eds.), Stable Isotopes in High Temperature Geological Processes. Mineralogical Society of America, Reviews in Mineralogy 16,165-184.

Tavares F.M., Klein E.L., Campos, L.D. 2017. Tectônica. In: Klein, E.L., Lopes, E.C.S., Tavares, F.M., Campos, L.D., Souza-Gaia, S.M., Neves, M.P., Perrotta, M.M. (eds) Áreas de Relevante Interesse Mineral: Cinturão Gurupi. Informe de Recursos Minerais, 11, Série Províncias Minerais do Brasil, Brasília, CPRM-Serviço Geológico do Brasil, 59-74.

Van der Kerkhof A., Thiéry, R. 2001. Carbonic inclusions. Lithos 55, 49–68.

Vennemann T.W., O'Neil, J.R. 1993. A simple and inexpensive method of hydrogen isotope and water analyses of minerals and rocks based on zinc reagent. Chemical Geololgy (Isotope Geosciences Section) 103, 227–234.

Wilkinson J.J. 2001. Fluid inclusions in hydrothermal ore deposits. Lithos 55, 229-272.

Witt W.K. 1993, Lithological and structural controls on gold mineralization in the Archaean Menzies-Kambalda area, Western Australia: Australian Journal of Earth Sciences, v. 40, p. 65–86.